Crash test for the restricted three-body problem

Jan Nagler
Institut für Theoretische Physik, Otto-Hahn-Allee, Universität Bremen, 28334 Bremen, Germany
(Received 8 September 2004; published 14 February 2005)

The restricted three-body problem serves to investigate the chaotic behavior of a small body under the gravitational influence of two heavy primary bodies. We analyze numerically the phase space mixing of bounded motion, escape, and crash in this simple model of (chaotic) celestial mechanics. The presented extensive numerical analysis reveals a high degree of complexity. We extend the recently presented findings for the Copenhagen case of equal main masses to the general case of different primary body masses. Collisions of the small body onto the primaries are comparatively frequent, and their probability displays a scale-free dependence on the size of the primaries as shown for the Copenhagen case. Interpreting the crash as leaking in phase space the results are related to both chaotic scattering and the theory of leaking Hamiltonian systems.

DOI: 10.1103/PhysRevE.71.026227 PACS number(s): 05.45.Ac, 05.45.Pq, 47.52.+j

I. INTRODUCTION

The restricted three-body problem (RTBP) is a simple model in celestial mechanics. It was first considered by Euler (1772) and Jacobi (1836) and has attracted much attention until today. Extensive investigations, analytical and numerical, are reported in the famous works of Szebehely [1–5] and Hénon [6–12]. Major parts of the standard reference of the RTBP deal with finding, describing, and classifying periodic orbits. However, the applications are ubiquitous. We mention only deterministic chaos [13], relativistic dynamics [14,15], quantum mechanics [16], and chemical [17,18] and astrophysical issues [19–21]. One reason for the diversity of applications may be the simplicity and cosmological relevance of the problem. It has been studied to investigate the stability of (extra)solar (sub)systems [22,23], (chaos assisted) asteroid capture [24], and the dynamics of two massive black holes orbited by a sun [25]. Although much simpler than the general three-body problem the RTBP is nonintegrable and serves as a paradigm for classical chaos [13].

For the Copenhagen case of equal main masses ($\mu=1/2$) we recently presented a partition of orbits into classes of various kinds of regular motion, chaotic motion, escape, and crash (see Ref. [26]). Therein we focused our attention mainly on retrograde orbits. Here we focus on both retrograde and direct orbits in the investigation of the phase space projection onto the configuration space. In addition, we extend the analysis to different values of the mass ratio μ.

The paper is organized as follows. In the next section we introduce the RTBP. Section III briefly reviews the classification scheme previously introduced in Refs. [26,27]. The scheme is important for the diagrams that represent the substantial numerical results in the present article. In Sec. IV the phase space mixing of the projection onto the configuration space is discussed for the Copenhagen problem. Section V extends the discussion to relevant values of the mass ratio $\mu\neq 1/2$. In Sec. VI we focus on the (x,E) plane (energy versus position) for different values of μ. An analysis of the dependence of the total area of crash on the primary sizes follows in Sec. VII. Finally, we summarize our findings in the conclusions.

II. THE MODEL

We investigate the (planar circular) restricted three-body problem. Two primary bodies move on different circles with the same Kepler frequency[1] about their common center of gravity (the origin) assumed to be fixed and a test body moves in the same plane (see Fig. 1).

In the inertial frame of reference the RTBP has a time-dependent potential $V_\mu(x,y,t)=-\mu/r_1(t)-(1-\mu)/r_2(t)$ where $\mu=m_1/(m_1+m_2)$, and $r_1(t),r_2(t)$ are the distances to the respective primaries. The time dependence of the potential is usually eliminated using a corotating frame wherein the primaries rest. In the corotating coordinate system $V_J=-\mu/r_1-(1-\mu)/r_2-\frac{1}{2}(x^2+y^2)$ where $r_1^2=(x+\mu)^2+y^2$, $r_2^2=(x-1+\mu)^2+y^2$, is the corresponding potential that Jacobi introduced first. Hence, it is called Jacobi's potential. The quadratic term results from the centrifugal force $F_{\text{cen}}=(x,y)$, whereas the Coriolis force $F_{\text{Cor}}=2(\dot{y},-\dot{x})$ gives no contribution to the potential. $E=\frac{1}{2}(\dot{x}^2+\dot{y}^2)+V_J$ is conserved and (up to the factor -2) has been known historically as Jacobi's integral $C=-2E$. Note that the energy in the inertial system E_{in} is the sum of E and the angular momentum L:

$$E_{\text{in}} = E + L. \tag{1}$$

It is widely believed that E is the only (independent) integral of the system [28]. The scaled equations of motion for the test body in the corotating frame read

$$\ddot{x} = 2\dot{y} + x - (1-\mu)\frac{x+\mu}{r_1^3} - \mu\frac{x-1+\mu}{r_2^3},$$

$$\ddot{y} = -2\dot{x} + y - (1-\mu)\frac{y}{r_1^3} - \mu\frac{y}{r_2^3}. \tag{2}$$

Note that in Eq. (2) the radius variables are no longer explicitly time dependent. In addition the equations of motion (2) are invariant under the symmetry operation $\Sigma:(x,y,t)\rightarrow(x,$

[1]The distance between the two primaries is scaled to unity and a time unit is related to the unit angular velocity of the primaries so that one rotation corresponds to 2π time units.

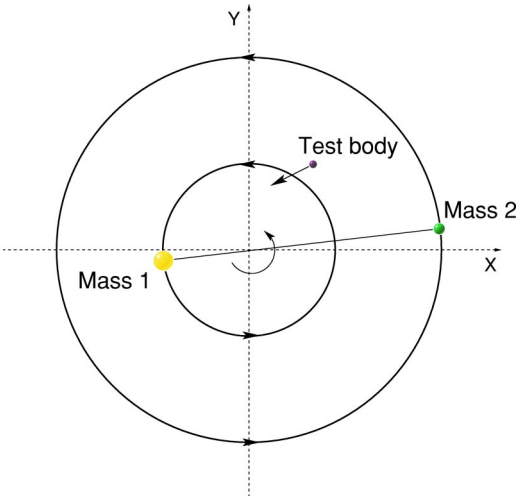

FIG. 1. (Color online) Schematic picture of the restricted three-body problem.

$-y,-t$). For the Copenhagen case ($\mu=1/2$) there is another special symmetry $\Sigma':(x,y,t)\rightarrow(-x,-y,t)$. These two are the only known (independent) symmetries of the equations of motion (2).

III. ORBIT TYPE DIAGRAMS

Due to Jacobi's integral the motion is restricted to three-dimensional surfaces $E=$const in phase space. We study the position and extent of chaos in terms of Poincaré sections being complete (in the sense of Dullin and Wittek [29]). With polar coordinates (r,ϕ) in the center of mass (COM) system of the corotating frame the condition $\dot{r}=0$ defines a two-dimensional surface of section in the surface $E=$const, with two disjoint parts $\dot{\phi}<0$ and $\dot{\phi}>0$. Each of these two parts has a unique projection onto the configuration space, i.e., the (x,y) plane. Figure 2 displays these projections for both $\dot{\phi}<0$, and $\dot{\phi}>0$, at two different energy levels.

In common representations of Poincaré sections the color codes indicate single orbits. In the Poincaré sections presented here each pixel is given a color according to the orbit *type*. We call these diagrams *orbit type diagrams* (OTDs). The orbit types are classified into bounded motion of a few kinds, unbounded motion, and collision orbits.

A. Bounded motion

For chaotic systems with configuration space extending to infinity it is a formidable task to distinguish bounded from unbounded motion for specific initial conditions. Here we use a practical definition of bounded motion: We call an orbit bounded if the test body stays confined for t_{timeout} inside the system's disk with radius R_{system} and center coinciding with the COM origin. This implies that the higher the values of t_{timeout} and R_{system}, the more adequate the statement *bounded motion* becomes. In the limit $t_{\text{timeout}}\rightarrow\infty$ the definition becomes the precise description of bounded motion in a disk of

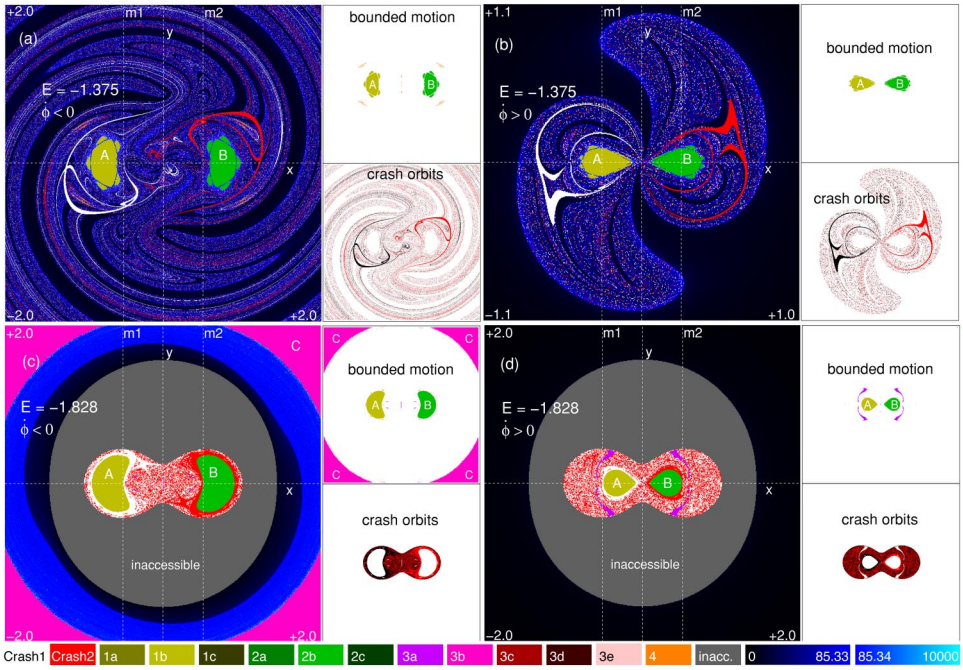

FIG. 2. (Color online) Orbit type diagrams (OTDs) for two different energy levels, and for both parts $\dot{\phi}<0$ and $\dot{\phi}>0$ of the surface of section $\dot{r}=0$. The (x,y) plane in a corotating frame of reference for the Copenhagen case (RTBP for $\mu=1/2$) is shown. Regions of bounded motion and collision are shown beside the OTDs. The color of a point represents the orbit type of a test body which has been launched with pericenter position at (x,y) for the energy level E (see orbit class legend below). Top: OTD and its decomposition at $E=-1.375$ for $\dot{\phi}<0$ (a), and for $\dot{\phi}>0$ (b). Bounded motion is indicated by the gray scales (colors) of classes 1a–4. White [black (red)] points indicate a collision with mass 1 (2). Escape orbits are colored black ($t_{\text{escape}}=0$) to gray (blue) ($t_{\text{escape}}=10\,000$). Bottom: Decompositions for $E=-1.828$: (c) $\dot{\phi}<0$, (d) $\dot{\phi}>0$. Positions of the primaries are indicated by $m1$ ($m2$). Radii of the primaries (not shown) $R_{\text{mass}_{1,2}}=10^{-4}$.

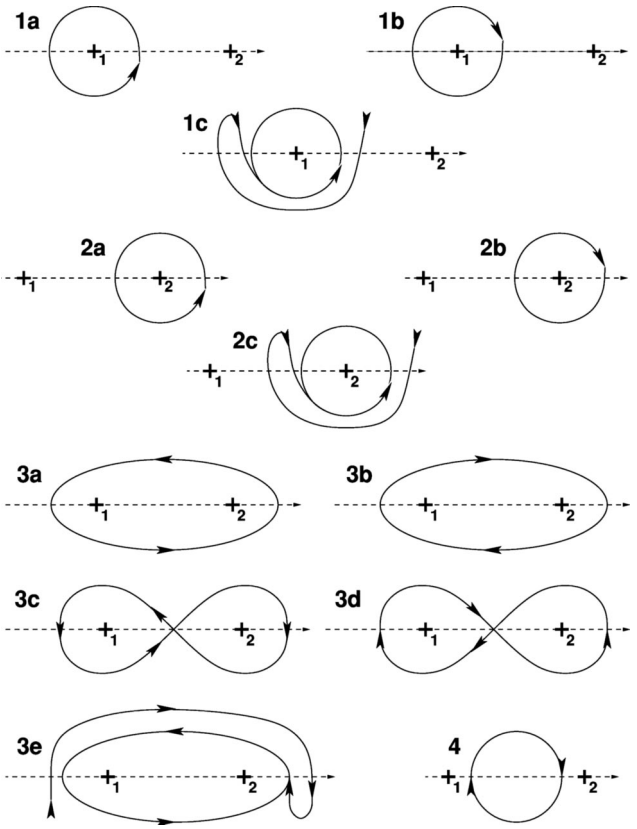

FIG. 3. Symbol sequences for the orbit examples: Class 1a, (LLL…; 000…); 1b, (RRR…; 000…); 1c, (R0LLL…; 000…). Class 2a, (000…; LLL…); 2b (000…; RRR…); 2c, (000…; R0LLL…). Class 3a, (LLL…; LLL…); 3b, (RRR…; RRR…); 3c, (L00LL00L…; 0RR00RR0…); 3d, (R00RR00R…; 0LL00LL0…); 3e, (R0LLL…; R0LLL…). Class 4, (000…; 000…). It is important to know that the orbits need not be periodic to have the same symbol sequences.

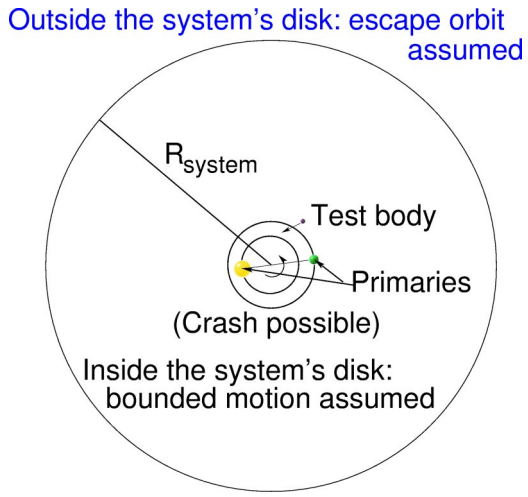

FIG. 4. (Color online) Schematic picture of the orbit classification. We call the motion bounded if the test body stays confined for a given time, say t_{timeout}, inside the system's disk with radius R_{system}. If the test body leaves the disk the integration is aborted and the motion is assumed to be unbounded. We call the corresponding trajectory an escape orbit. Finally, if during the integration a crash with one of the main masses occurs we call the trajectory a crash orbit.

radius R_{system}. Unfortunately, the higher the values of these two parameters, the longer the numerical integration takes. In this article, we choose $t_{\text{timeout}}=10\,000$ and $R_{\text{system}}=10$. It is important to know that a lower value of t_{timeout} smooths the fractal border of bounded regions [27]. Our symbolic orbit classification for bounded motion is suitable for an automatic identification of the orbit types. The classification differs from the standard scheme introduced by Strömgren and extended by Hénon (see, e.g., Hagihara [30] for a detailed discussion). We emphasize the distinction between regular motion (including small scale chaos and quasiperiodic motion) on the one side and strongly chaotic motion (not hindered by Kolmogorov-Arnol'd-Moser orbits [13]) on the other. Our classification is based on an automatic detection of x axis passages of the test body. Two consecutive x axis passages define a *half rotation* with respect to the fixed positions of the primaries. We name a half rotation counterclockwise around one (of the two) primaries by "L," a half rotation clockwise by "R," and effectively no rotation is labeled by zero "0." For example, a quasiperiodic clockwise orbit *solely* around the second center is described by the two symbol sequences (000…; RRR) (cf. class 2b in Fig. 3). Note that the left slot of the bracket refers to revolutions around the first main mass and the right to those around the second primary body. In Fig. 3 we show example orbits for 12 classes that we termed 1a–4. A precise description of the classes has been given earlier [27].

B. Unbounded motion (escape orbits)

If the test body leaves the system's disk (with radius R_{system}) at a time $t_{\text{escape}}<t_{\text{timeout}}$, we say that the test body has left the system and stop the numerical integration. These points in the OTDs are colored from dark gray (blue) (corresponding to a small value of t_{escape}) to light gray (blue) (a high value of t_{escape}).

One should keep in mind that the Kepler problem exhibits ellipses for all starting positions in the configuration space (x,y) for some energy level. Thus, our definition is inappropriate for orbits that never enter the *inner* region, say, $r\lesssim 1$, being only slightly disturbed Kepler ellipses. But here we focus our attention on the dynamics of the motion in the inner region. Furthermore, thinking of a real solar system which possesses more disturbing bodies, the definition is physically motivated.

C. Collision

A crash with the first primary body of radius R_{mass_1} simply occurs when the test body, being a point mass, crosses the disk with radius R_{mass_1} around mass 1. In the OTDs these points are colored white. A collision with the second primary body (with radius R_{mass_2}) is defined analogously but colored gray (red). Figure 4 displays a schematic picture of the orbit classification.

In order to keep things simple we assume the simple relation

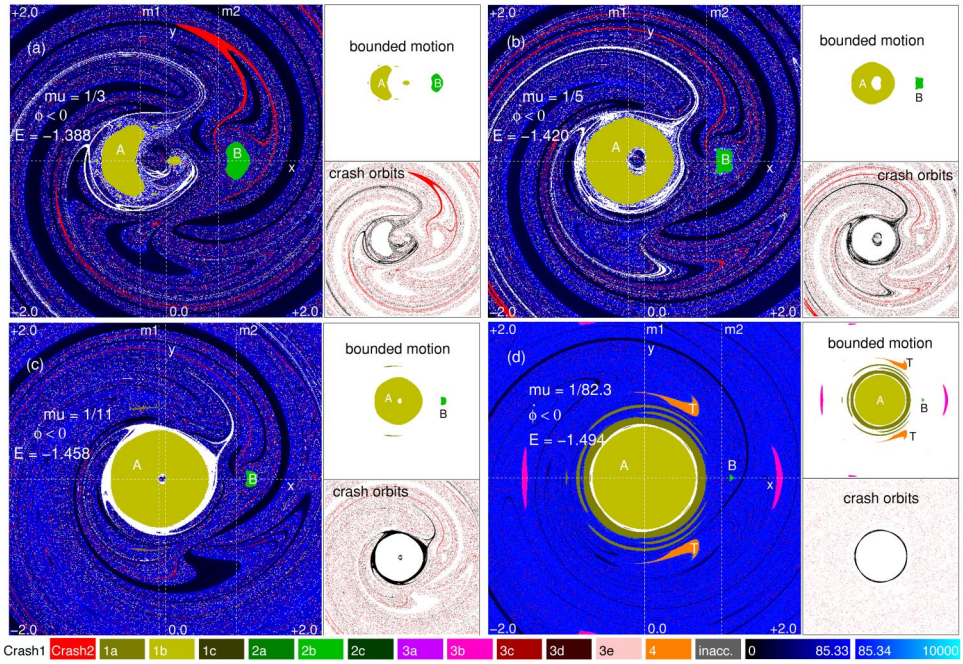

FIG. 5. (Color online) Orbit type diagrams for different values of the mass ratio μ at the respective Trojan energy levels $E=V_T(\mu)$, and for $\dot{\phi}<0$. Regions of bounded motion and collision are shown beside the OTDs. The color of a point represents the orbit type of a test body which has been launched with pericenter position at (x,y) (see orbit class legend below). (a) OTD and its decomposition for $\mu=1/3$ at $E=V_T(1/3)=-1.388$. Bounded motion is indicated by the gray scales (colors) of classes 1a–4. White [black (red)] points indicate a collision with mass 1 (2). Escape orbits are colored black ($t_{\text{escape}}=0$) to gray (blue) ($t_{\text{escape}}=10\,000$). Radii of the primaries (not shown) $R_{\text{mass}_1}=10^{-4}$, $R_{\text{mass}_2}=R_{\text{mass}_1}(2\mu)^{1/3}=0.874\times10^{-4}$ [see text around Eq. (3)]. (b) Decompositions for $\mu=1/5$ at $E=V_T(1/5)=-1.420$, $R_{\text{mass}_2}=0.737\times10^{-4}$. (c) Decompositions for $\mu=1/11$ at $E=V_T(1/11)=-1.458$, $R_{\text{mass}_2}=0.567\times10^{-4}$. (d) Decompositions for $\mu=1/82.3$ (value for the earth-moon system) at $E=V_T(1/82.3)=-1.494$, $R_{\text{mass}_2}=0.290\times10^{-4}$. Positions of the primaries are indicated by $m1$ ($m2$).

$$R_{\text{mass}_2}=R_{\text{mass}_1}\times(2\mu)^{1/3} \tag{3}$$

between the radii of the primaries. First, Eq. (3) guarantees $R_{\text{mass}_2}=R_{\text{mass}_1}$ for $\mu=1/2$, and second, it mimics the assumption that the radius of a celestial body is proportional to the cubic root of its mass. If not stated otherwise we choose here $R_{\text{mass}_1}=10^{-4}$ corresponding roughly to the (scaled) relations of the sun-jupiter system where $\mu\approx1/1000$.

IV. THE (x,y) PLANE FOR THE COPENHAGEN CASE

Figure 2 shows OTDs for the Copenhagen case $\mu=1/2$. The (x,y) plane (in the corotating frame of reference) for the surface of section $\dot{r}=0$ with respect to the origin (0,0) for two different energy levels is shown. The diagrams in Fig. 2 exhibit the symmetry Σ' because it is also respected by the section condition.

Figure 2(a) shows the OTD decomposition for both $\dot{\phi}<0$ and $\dot{\phi}>0$ at energy $E=-1.375$ in comparison. For $\mu=1/2$ the energy level $E=-1.375$ represents the so-called Trojan energy $V_T(\mu)=-(3/2)+(\mu(1-\mu)/2)$ corresponding to the maxima of Jacobi's potential. Thus, the test body has access to the full (x,y) plane.

The main region A of bounded motion around mass 1 consists of a central region, surrounded by six (five small and one tiny) islands. For each region of regular motion there is a resonance, i.e., a periodic orbit at its center. The regions in white (black) represent the start positions where the test body eventually crashes with the first primary body. Due to the rotating primaries these *crash basins* wind out as spirals in the outer regions of the diagram. But there also appear crash basins in the immediate neighborhood of the origin. Strikingly, the area of crash basins is several orders of magnitude greater than the total size of the main body disks. In this representative Poincaré section, the phase space emerges as a close mix of crash basins, regions of bounded motion, and escape basins. In the OTD for $\dot{\phi}>0$ at the Trojan energy level $E=-1.375$, escape dominates the configuration space. The total size of regions of bounded motion is less for $\dot{\phi}>0$ than for $\dot{\phi}<0$. This can be understood in terms of Eq. (1). The energy in the inertial system E_{in} is higher for L positive than for negative values of L.

In Fig. 2(c) we depict the (x,y) plane for $\dot{\phi}<0$ at $E=-1.828$. There is an inaccessible region (gray) in the plane because the energy is smaller than the Trojan energy. The inaccessible area separates two regions. In the outer region there is a (partly visible) ring of bounded motion (C) which separates regions of escape orbits. In the inner zone the test body is confined. The regions A and B indicate stable motion around the individual primaries. These regions are surrounded by a chaotic mix of areas of crash orbits with respect to the first and the second primary bodies. In Fig. 2(d) the OTD for the condition $\dot{\phi}>0$ is shown. In addition to the main regions of bounded motion A and B, there are four

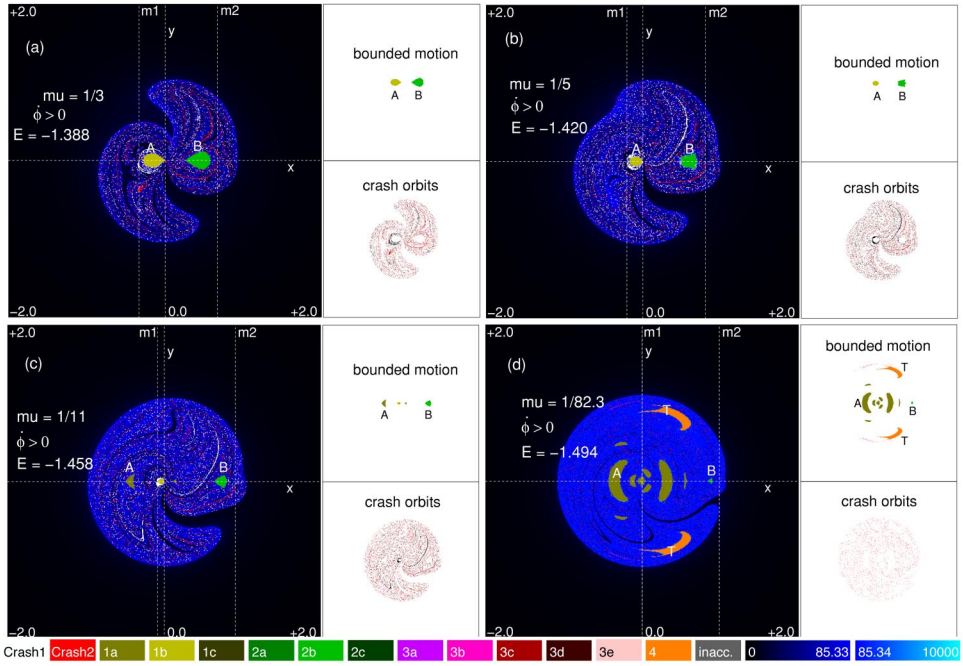

FIG. 6. (Color online) Orbit type diagrams for different values of the mass ratio μ at the respective Trojan energy levels $E=V_T(\mu)$, and for $\dot{\phi}>0$. Regions of bounded motion and collision are shown beside the OTDs. The color of a point represents the orbit type of a test body which has been launched with pericenter position at (x,y) (see orbit class legend below). (a) OTD and its decomposition for $\mu=1/3$ at $E=V_T(1/3)=-1.388$. Bounded motion is indicated by the gray scales (colors) of classes 1a–4. White [black (red)] points indicate a collision with mass 1 (2). Escape orbits are colored black ($t_{\text{escape}}=0$) to gray (blue) ($t_{\text{escape}}=10\,000$). (b) Decompositions for $\mu=1/5$ at $E=V_T(1/5)=-1.420$. (c) Decompositions for $\mu=1/11$ at $E=V_T(1/11)=-1.458$. (d) Decompositions for $\mu=1/82.3$ (value for the earth-moon system) at $E=V_T(1/82.3)=-1.494$. Positions of the primaries are indicated by $m1$ ($m2$). Radii of the primaries, see legend of Fig. 5, according to Eq. (3).

main regions of stable type-3a trajectories [gray (violet)].

The OTDs in Fig. 2 possess both smooth (nonfractal) and fractal regions of the boundaries which separate the regions of escape orbits and the crash basins. In the context of *leaking* Hamiltonian systems the boundaries are classified to be of type II [31–33]. Here, the leakages are defined by the crash conditions and the escape condition, resulting in three *exit modes*. Due to the complexity of the boundaries it is difficult to predict whether the test particle (e.g., an asteroid or a satellite) hits a primary body or leaves the (solar) system.

Note that the OTDs differ only slightly from those obtained using a suitably defined escape velocity condition, e.g., $\dot{r}>[2/(r-1)]^{1/2}$, rather than the escape condition $r>R_{\text{system}}$ used here. As a consequence, the occurrence of *escape basins* [colored solid dark gray (blue)] is not an artifact of the arbitrarily chosen escape condition.

V. THE (x,y) PLANE FOR $\mu<1/2$

So far we have discussed (and partly reviewed) the dynamics of the Copenhagen case of the RTBP. In this section we extend our investigations to the case for $\mu<1/2$.

A. Retrograde passage through extremal distances

Figure 5 shows OTDs for various values of the mass ratio μ, and for $\dot{\phi}<0$. For $\mu\neq 1/2$ the origin does not coincide with the first Lagrangian point L_1 as for the Copenhagen case. The diagrams exhibit no longer the symmetry Σ'.

In Fig. 5(a) the main part of bounded motion A is fragmented. Due to the smaller mass 2 ($\mu=1/3$) the region of stability with respect to mass 2, B, is smaller than the total size of bounded motion around mass 1. In the (x,y) plane for $\mu=1/5$, Fig. 5(b), the region A resembles a section of a torus. The central hole *survives* for all ratios $\mu<1/5$, [see Figs. 5(c) and 5(d)], even though too small to be visible in Fig. 5(d). Note that in the limit $\mu\to 0$ the (x,y) plane becomes symmetric to the x axis.

From Fig. 5(a) to Fig. 5(d) crash on the second primary body [gray (red)] becomes more and more unlikely. The shrinking total size of the crash basins with respect to the less heavy main body 2 is mostly due to its decreasing mass, and in addition but with minor significance, due its decreasing radius R_{M_2}. In Fig. 5(c) the crash basins of the first primary body (white and black) separate bounded motion (A) from the bulk regions where escape dominates. For a smaller value of the mass ratio $\mu=1/82.3$, Fig. 5(d), the central crash basin region around A separates bounded motion of type 1b from stable motion of type 1a. For $\mu<\frac{1}{2}(1-\sqrt{23/27})\approx 0.0385\ldots$ the RTBP exhibits stable trajectories around the Trojan points, i.e., the maxima of V_J. In Figs. 5(d) and 6(d) the corresponding regions of stability (T) are colored gray (orange).

Another observation is that statistically escape orbits need more time to leave the system the smaller the mass ratio.

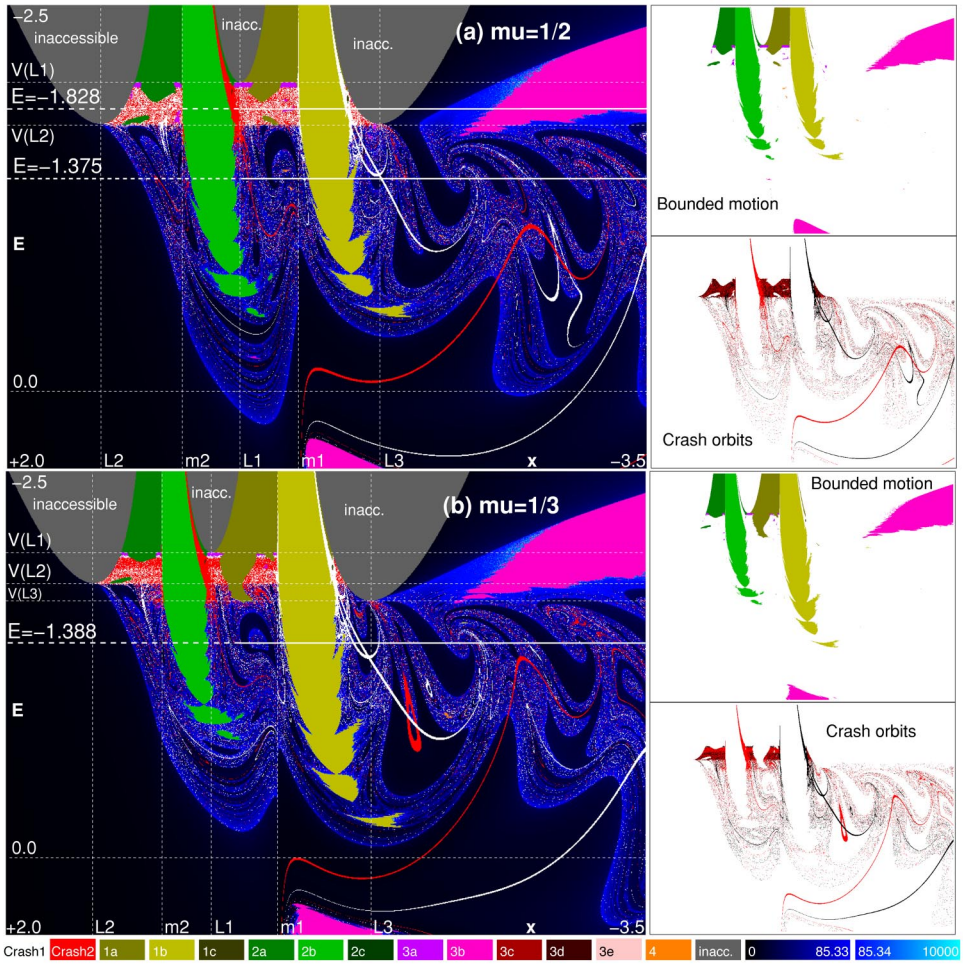

FIG. 7. (Color online) Orbit type diagrams for the (x,E) plane for the Copenhagen case $\mu=1/2$ (a), and for $\mu=1/3$ (b). Poincaré section, $y=\dot{x}=0$, $\dot{y}>0$. The symbols $L_{1,2,3}$ represent the x positions of the corresponding Lagrange points and $V_J(L_{1,2,3})$ are their potential values. In addition, the energy levels for the corresponding (x,y) diagrams are highlighted. The smaller panels show the decomposition into bounded motion and crash orbits of the corresponding OTD. Crash onto primary 1, black; crash onto primary 2, gray (red). Radii of the second primary body according to Eq. (3) for $R_{\text{mass}_1}=10^{-4}$ (see also legend of Fig. 5).

Hence the crash basins [gray (blue)] are lighter the smaller μ. The increasing size of regions of bounded motion (the smaller μ) indicates an increasing tendency toward boundedness of the test body the greater the first mass, i.e., the smaller μ.

The smaller μ the closer the position of mass 1 wanders to the origin. Because the test body is launched perpendicularly to the radius vector, i.e., $\dot{r}=0$, crash onto mass 1 becomes rarer for small values of μ than for bigger values. Strikingly, in Figs. 5(d) and 6(d) ($\mu=1/82.3$), crash onto mass 1 (white and black) disappears completely for both $\dot{\phi}>0$ and (up to the white ring) for $\dot{\phi}<0$.

In this paragraph we focused on the phase space projection onto the configuration space for $\dot{\phi}<0$ excluding a major part of direct motion in the inertial frame of reference. However, in the context of celestial mechanics it is more natural to investigate satellites that corotate with the primaries, i.e., $\dot{\phi}_{\text{in}}>0$, implying for simple corotating stable orbits $\dot{\phi}>0$ (in the corotating frame).

B. Direct passage through extremal distances

In Fig. 6 we depict OTDs for the same values of the mass ratio μ as before but for $\dot{\phi}>0$ passages. Strikingly, escape dominates the (x,y) plane (cf. Fig. 5). The escape basins [black (dark blue)] represent orbits that leave the system after a short transient time corresponding to small values of t_{escape}. As mentioned before, this can be understood in terms of Eq. (1). The greater the radius r the greater the energy in the inertial system. Thus, in contrast to the OTDs for $\dot{\phi}<0$, there appears a border between possible nonescaping orbits [(light) gray (blue)] and a region of escape only (black). Consequently, the black region represents orbits that move (in the corotating system), spiraling out of the system without entering the inner region.

VI. THE (x,E) PLANE

The diagrams for the (x,y) plane provide information on the phase space mixing for only a fixed energy and for orbits

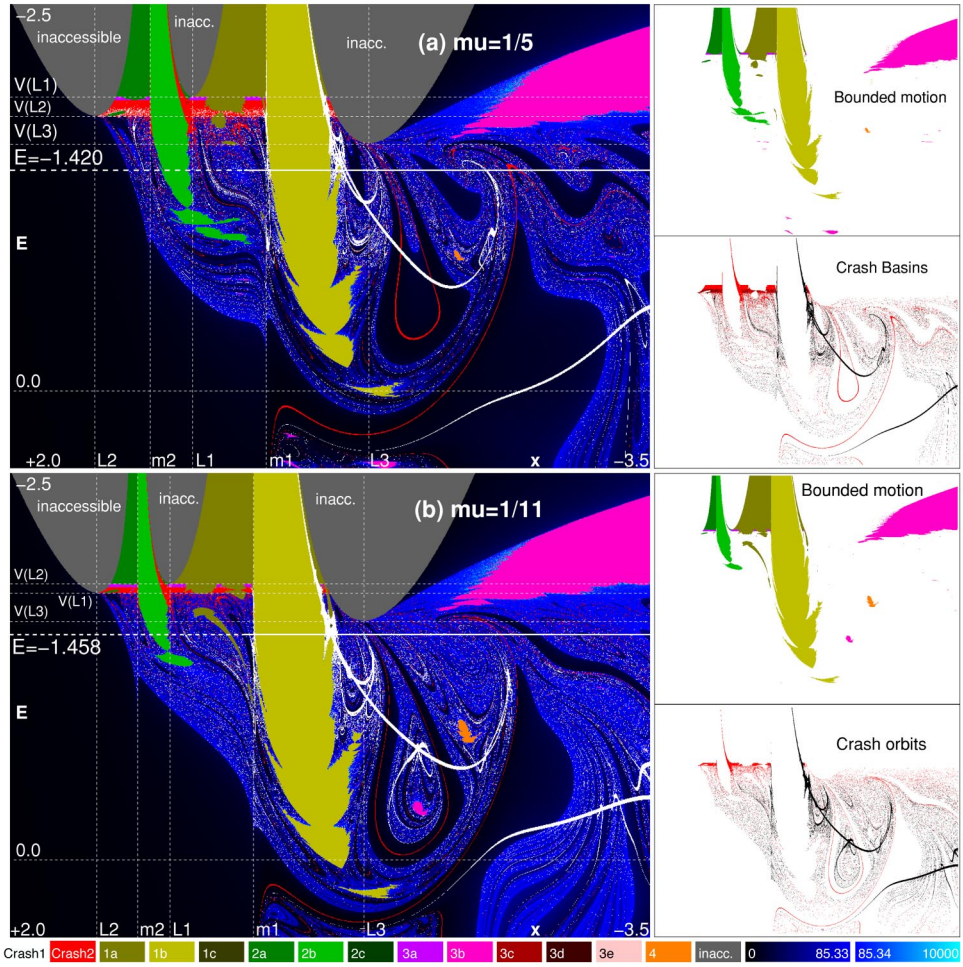

FIG. 8. (Color online) Orbit type diagrams for the (x,E) plane for $\mu=1/11$ (top) and $1/3$ (bottom). Poincaré section, $y=\dot{x}=0$, $\dot{y}>0$. Radii of the primaries, $R_{\text{mass}}=10^{-4}$. The symbols $L_{1,2,3}$ represent the x positions of the corresponding Lagrange points and $V_J(L_{1,2,3})$ are their potential values. In addition, the energy levels for the corresponding (x,y) diagrams are highlighted. The smaller panels show the decomposition into bounded motion and crash orbits of the corresponding OTD. Crash onto primary 1, black; crash onto primary 2, gray (red). Radii of the second primary body according to Eq. (3) for $R_{\text{mass}_1}=10^{-4}$ (see also legend of Fig. 5).

that transverse the surface of section either directly or retrogradely. For the Copenhagen problem Hénon considered a plane that provides information about regions of stability and regions of escape orbits using the section (of a Poincaré section) $y=\dot{x}=0$, $\dot{y}>0$, i.e., the test body starts on the x axis, parallel to the y axis, and in the positive y direction. Thus, in contrast to the section discussed before, only orbits with pericenters on the x axis are included. But then the energy E is used as ordinate. In the (x,E) plane the corresponding orbits transverse the x axis in both directions, retrogradely (for $x<0$) and directly (for $x>0$). In Fig. 7 the (x,E) plane for the Copenhagen case (a) and $\mu=1/3$ (b) are displayed. The energy $E=-C/2$ increases downward and x decreases from the left to the right. In the (x,E) diagrams the energy levels for the corresponding (x,y) planes that we depict in Figs. 2, 5, and 6 are also displayed. For the respective mass ratios μ the line $(x<0,E)$ in the (x,E) diagram is equivalent to the line $(x<0,y=0)$ in the (x,y) OTD for the energy level E and $\dot{\phi}<0$. Vice versa, for $\dot{\phi}>0$ the lines $(x>0,E)$ in the (x,E) plane and $(x>0,y=0)$ in the (x,y) OTD at energy E are also equivalent. In the respective (x,E) diagrams the fat dashed line indicates the energy level $E=V_T(\mu)$ for $x>0$ whereas the fat solid line for $E=V_T(\mu)$ represents the part for $x<0$ (cf. Figs. 2–9).

In the region between the potential values of the first two Lagrange points $V_{L_{1,2}}$ the test body is confined. The region shows many tiny islands of regular motion plus a chaotic mix of areas of crash orbits (cf. OTDs for $E=-1.828$ in Fig. 2). From chaos theory we expect indeed an infinite number of islands of (stable) quasiperiodic (or small scale chaotic) motion.

Due to the symmetry Σ' for $\mu=1/2$ crash onto mass 1 and mass 2 is equally frequent. For $\mu<1/2$ symmetry Σ' vanishes. Thus the potential values at L_2 and L_3, i.e., V_{L_2} and V_{L_3}, no more coincide. As a consequence between the energy levels V_{L_2} and V_{L_3} the test body can pass L_2, but not L_3. In (x,y) OTDs for the region $V_{L_2}\leqslant E\leqslant V_{L_3}$ this results in a C-shaped inaccessible region which is open on the right hand side (not shown).

Figure 9 displays the (x,E) plane for $\mu=1/82.3$. The eye-catching white bands (B) represent orbits that practically immediately collide with the first primary body. For $\mu\to 0$ the

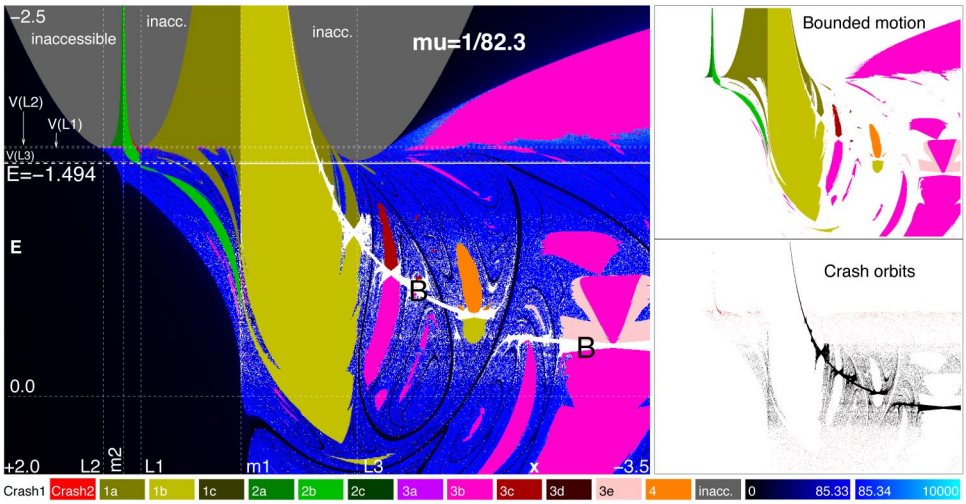

FIG. 9. (Color online) Orbit type diagrams for the (x,E) plane for $\mu=1/82.3$ (earth-moon system). Poincaré section, $y=\dot{x}=0$, $\dot{y}>0$. The symbols $L_{1,2,3}$ represent the x positions of the corresponding Lagrange points and $V_J(L_{1,2,3})$ are their potential values. In addition, the energy levels for the corresponding (x,y) diagrams are highlighted. The smaller panels show the decomposition into bounded motion and crash orbits of the corresponding OTD. Crash onto primary 1, black; crash onto primary 2, gray (red). Radii of the primaries, $R_{\text{mass}_1}=10^{-4}$, $R_{\text{mass}_2}=0.290\times10^{-4}$.

bands become a smooth curve which represents all orbits with vanishing angular momentum in the inertial system [13].

As seen in the previous section for decreasing μ the area of crash orbits with respect to mass 2 shrinks (compare Figs. 7–9), the area representing bounded motion around the first primary (classes 1a–1c) grows, whereas the size of regions of bounded motion around the second primary decreases (classes 2a–2c).

On the one hand, for the investigated range and resolution, the OTDs for the (x,E) plane possess the more islands of bounded motion the smaller μ. On the other hand the boundaries between bounded motion and escape appear to become smoother for a decreasing mass ratio. This can be understood if we recall that $\mu=0$ is an integrable case (being Kepler's problem) of the RTBP. A stronger magnification of the occurring small-scale chaos is needed to visualize the fractal boundaries in the neighborhood of the integrable case. We refer to the literature for a more detailed discussion of Hill's case $\mu\to0$ where, in contrast to here, the moon is the test body in a scaled limiting case of the sun-earth potential [10–13,34,35].

A detailed discussion of the (x,E) planes incorporating bifurcations of periodic orbits, etc., will be presented elsewhere [36].

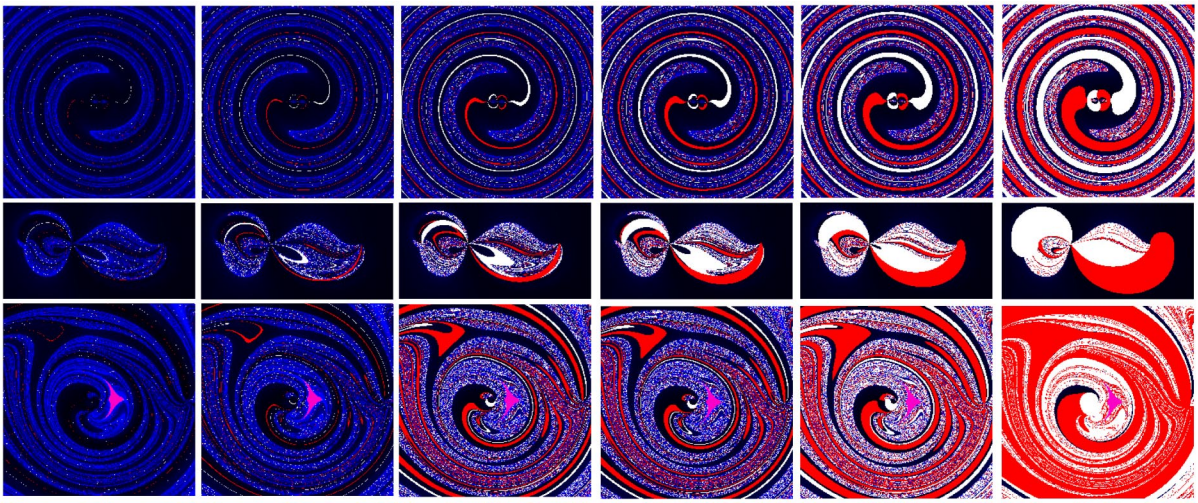

FIG. 10. (Color online) Extension of the crash basins [white and gray (red)] for different radii of the primary bodies. Orbit type diagrams for the (x,y) plane for $\mu=1/2$, $1/3$, and $\mu=1/11$ at different energy levels are shown. Surface of section condition, $\dot{r}=0$. Radii of the primaries (from left to right): R_{M_1} 10^{-5}; $10^{-3.5}$, $10^{-2.5}$, 10^{-2}, $10^{-1.5}$, 10^{-1}. Radii of the second primary body according to Eq. (3). Top: $\mu=1/2$, $E=-0.1$, $\dot{\phi}<0$, $x,y=-5.0,\ldots,5.0$. Middle: $\mu=1/3$, $E=-0.6$, $\dot{\phi}>0$, $x=0.5,\ldots,1.9$, $y=-0.4,\ldots,1.1$. Bottom: $\mu=1/11$, $E=0.1$, $\dot{\phi}<0$, $x,y=-1.0,\ldots,1.0$. See Fig. 9 for the color legend.

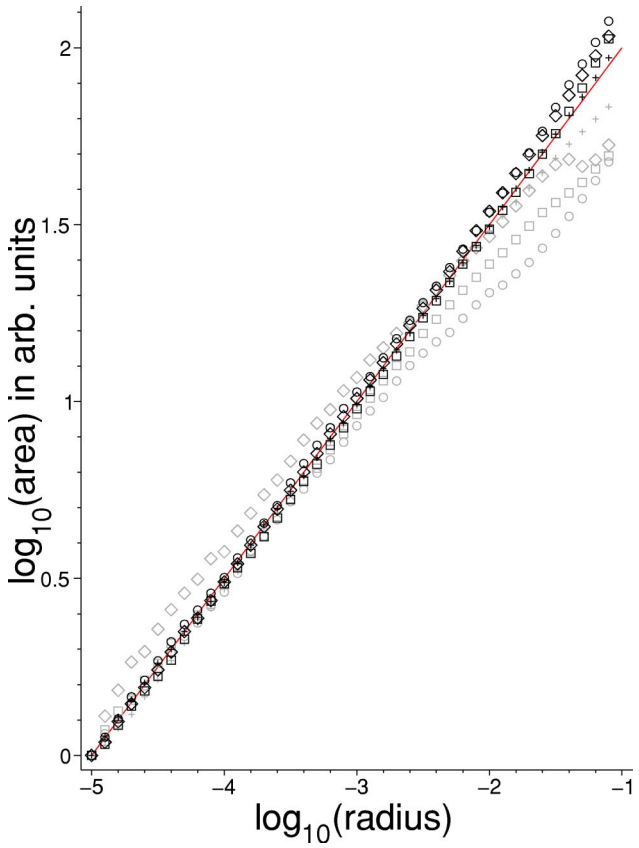

FIG. 11. (Color online) Log-log plot of the total size of crash onto mass 2 in the (x,y) plane for various ranges and for various values of μ and energy levels in arbitrary units versus the primary body radius $R_{M_1}=10^{-5},\ldots,10^{-1}$. Data are presented for both parts of the section $\dot{r}=0$, i.e., $\dot{\phi}<0$ (symbols in black) and $\dot{\phi}>0$ (symbols in gray). $\mu=1/2$ (crosses), $1/3$ (boxes), $1/5$ (circles), $1/11$ (diamonds). Gray (red) line, theoretical law, $A_{\text{crash}}\sim R^{1/2}$. Ranges: energy levels, $\mu=1/2$, $\dot{\phi}<0$, $x,y=-5.0,\ldots,5.0$, $E=-0.1$; $\dot{\phi}>0$: $x=-0.75,\ldots 0.75, y=-0.4,\ldots,0.35$, $E=-0.5$; $\mu=1/3$, $\dot{\phi}<0$, $x,y=-2.0,\ldots,2.0$, $E=0.0$, $\dot{\phi}>0$, $x=-0.5,\ldots,0.9, y=-0.4,\ldots,0.3$, $E=-0.6$; $\mu=1/5$, $\dot{\phi}<0$, $x,y=-2.0,\ldots,2.0$, $E=0.25$; $\dot{\phi}>0$, $x=-0.5,\ldots,1.0, y=-0.4,\ldots,0.35$, $E=-0.75$; $\mu=1/11$, $\dot{\phi}<0$, $x,y=-1.0,\ldots,1.0$, $E=0.1$; $\dot{\phi}>0$, $x,y=-0.3,\ldots,+0.2$, $E=-0.5$. The curves are arbitrarily normalized.

VII. SCALING LAW FOR THE CRASH BASINS

In the previous sections for a given mass ratio the radii of the primaries were arbitrarily fixed. In earlier investigations [26,27] we found a power law dependence of the total size of crash basins on the primaries' radii for different OTD planes and mass ratios. We now extend the analysis to the (x,y) plane for the mass ratios discussed so far in this article. Furthermore, the part $\dot{\phi}>0$ for the section condition $\dot{r}=0$ is included in the analysis and compared with the results for $\dot{\phi}<0$. Figure 10 displays OTDs at fixed energy for R_{M_1} increasing from 10^{-5} to 10^{-1} for three different values of the mass ratio.

For different mass ratios and energy levels Fig. 11 shows in a log-log plot the dependence of the total area of crash onto mass 2 versus the mass radius R_{M_1}. The total area of crash orbits follows approximately a power law over several orders of magnitude: $A_{\text{crash}}\sim R^{\alpha}$ with $\alpha\approx 0.5$.

In [26] we derived an approximation for the power law behavior $A_{\text{crash}}(R)\sim R^{\beta}$ with the exponent $\beta=1/2$. The scale-free behavior is slightly better reproduced for $\dot{\phi}<0$ than for $\dot{\phi}>0$. For big values of R_{M_1} the curves obtained from numerical calculations deviate from the theoretical result due to finite size effects. Note that one obtains similar graphs for the total area of crash onto mass 1, i.e., $A_1(R_{M_1})$, or the sum $A_{1+2}(R_{M_1})$, for various ranges, and values of energy level and mass ratio (not shown).

In the following we briefly review the analytical calculation. The RTBP can be (roughly) approximated by the Kepler problem when the test body is close to one primary body (just before a crash occurs), and in addition, when the rotation of the primaries is neglected. Using Eq. (1) from Kepler's ellipse formula we obtain

$$E=-\frac{1}{r_a+r_p}\mp\sqrt{\frac{2r_p r_a}{r_p+r_a}}, \tag{4}$$

where r_p denotes the perihelion and r_a the aphelion distance. Solving Eq. (4) for r_a yields

$$r_a(r_p)=-r_p-\frac{E+r_p^2}{E^2-2r_p}-\frac{\sqrt{r_p^4+2Er_p^2+2r_p}}{E^2-2r_p}. \tag{5}$$

A collision occurs when the test body intersects the disk with radius R around the Kepler singularity: $r_p\leqslant R$. Thus, for $R\ll 1$ the area of crash orbits can be approximated by $A_{\text{crash}}(R)\approx 2\pi r_a(0)\,[r_a(0)-r_a(R)]$. But for $r_p\ll 1$ Eq. (5) is approximated by $r_a(r_p)\approx -1/E+\sqrt{2r_p}/E^2$. Hence, we obtain a power law $A_{\text{crash}}(R)\sim R^{\beta}$ with the exponent $\beta=1/2$.

VIII. CONCLUSIONS

In conclusion, the orbit type diagrams that we presented in this article provide detailed information about the extent and position of bounded, unbounded, and crash orbits. We have numerically calculated more than 10 000 OTDs where in each diagram from about 32 000 up to 1×10^6 trajectories were evaluated. The extensive numerical analysis extends known behavior in the RTBP. In contrast to our own previous published studies [26,27] the numerical results presented here are based on the DKD (drift-kick-drift) leapfrog symplectic integrator of sixth order developed by Yoshida [37]. After testing various other integrators we consider this one as one of the most efficient for the RTBP if applied for extended phase space with a time step function corresponding to a *logarithmic Hamiltonian*, i.e., the case $\gamma=1$ in Ref. [38]. As a consequence we could improve both the accuracy and the computation speed. We have validated our numerics by monitoring the energy deviation from E during the integration, taking various step sizes, and choosing different integration parameters and ranges for comparison. Although the integration procedure disregards the system's symmetries, they are reproduced in the individual diagrams. Finally, boundary pixels in the presented OTDs were checked with increased accuracy.

It is important to know that the Poincaré sections discussed for the phase space projection onto the configuration space are not arbitrary but complete (in the sense of Dullin and Wittek [29]). Every trajectory must intersect the surface of section.

If crash is interpreted as a *leakage* in phase space the findings are examples of leaking Hamiltonian systems [33,39,40]. From that part of chaotic scattering theory it follows that the boundaries between the crash basins and the regions of escape orbits represent the *chaotic saddle* (i.e., the invariant manifolds) better the smaller the leakage (i.e., the primary disks). In that way the crash basins are connected to the foliation of phase space. In 1988 Bleher *et al.* [31] proposed the RTBP as an interesting application for a leaking Hamiltonian system. After discussing the Copenhagen problem in this context [26] we have now extended the analysis to the RTBP for values of the mass ratio different from $\mu = 1/2$. As expected from our findings and predictions of others [32], the boundaries between regions of crash and escape orbits emerge as so-called type II boundaries.

Due to the extended primaries the model is more applicable to realistic situations of celestial body problems than the pure RTBP. We analyzed the model for relevant mass ratios as the earth-moon system ($\mu = 1/82.3$), and for values investigated by Darwin ($\mu = 1/11$), Moulton ($\mu = 1/5$), and Jefferys ($\mu = 1/3$) [41]. Compared with the literature our results reveal a high degree of complexity that could not be accomplished in earlier days of computer power.

On the one hand the crash basins as part of the diagrams are more widely extended than one would naively expect. On the other hand the power law behavior compares with that found in the Copenhagen problem. The results show for $\mu < 1/2$ how comparatively small primaries affect regions of crash orbits. Moreover, for various mass ratios we found a power law dependence of the total size of crash on the primary radii. This result agrees with a calculation based on Kepler's ellipse formula that approximately predicts the simple relation $A(R) \sim R^{\beta}$ with $\beta = 1/2$ [26]. However, we would like to highlight that quantitatively a power law behavior with exponent $1/2$ is better reproduced the less the corresponding OTD possesses bounded motion.

Finally, the high degree of complexity in the diagrams suggests that the long term prediction in comparable celestial systems may become a formidable task.

ACKNOWLEDGMENTS

I warmly acknowledge P. H. Richter for the careful reading of the manuscript and T. Tél for fruitful discussions.

[1] V. Szebehely, *Theory of Orbits* (Academic Press, New York, 1967).
[2] V. Szebehely, Fundam. Cosmic Phys. **4**, 73 (1978).
[3] V. Szebehely and R. McKenzie, Celest. Mech. **23**, 131 (1981).
[4] J. Lundberg, V. Szebehely, R. S. Nerem, and B. Beal, Celest. Mech. **36**, 191 (1985).
[5] R. H. Smith and V. Szebehely, Celest. Mech. Dyn. Astron. **56**, 409 (1993).
[6] M. Hénon, Ann. Astrophys. **28**, 499 (1965).
[7] M. Hénon, Ann. Astrophys. **28**, 992 (1965).
[8] M. Hénon, Bull. Astron. **1**, 57 (1966).
[9] M. Hénon, Bull. Astron. **1**, 49 (1966).
[10] M. Hénon, Astron. Astrophys. **1**, 223 (1969).
[11] M. Hénon, *Generating Families in the Restricted Three-Body Problem* (Springer, Berlin, 1997).
[12] M. Hénon, *Generating Families in the Restricted Three-Body Problem. II. Quantitative Study of Bifurcations* (Springer, Berlin, 2001).
[13] P. H. Richter, Rev. Mod. Astron. **14**, 53 (2001).
[14] T. I. Maindl and R. Dvorak, Astron. Astrophys. **290**, 335 (1994).
[15] V. A. Brumberg, Celest. Mech. Dyn. Astron. **85**, 269 (2003).
[16] B. L.G. Bakker and R. van Dantzig, *Few-Body Problems in Physics '93* (Springer, New York, 1994).
[17] A. F. Brunello, T. Uzer, and D. Farrelly, Phys. Rev. A **55**, 3730 (1997).
[18] E. Lee, A. F. Brunello, and D. Farrelly, Phys. Rev. A **55**, 2203 (1997).
[19] M. A. Murison, Astrophys. J. **98**, 2346 (1989); Astrophys. J. **98**, 2383 (1989).
[20] N. Haghighipour, Mon. Not. R. Astron. Soc. **304**, 185 (1998).
[21] N. Haghighipour, Mon. Not. R. Astron. Soc. **316**, 845 (1999).
[22] J. Liebert and W. B. Hubbard, Nature (London) **400**, 316 (1999).
[23] J. J. Lissauer, Nature (London) **419**, 355 (2002).
[24] S. A. Astakhov, A. D. Burbanks, S. Wiggins, and D. Farrelly, Nature (London) **423**, 264 (2003).
[25] G. D. Quinlan, New Astron. **1**, 35 (1996).
[26] J. Nagler, Phys. Rev. E **69**, 066218 (2004).
[27] J. Nagler, Ph.D. thesis, Universität Bremen, 2002.
[28] H. Poincaré, *Les Méthodes Nouvelles de la Mécanique Céleste* (Gauthier-Villars, Paris, 1892) [English translation, *History of Modern Physics and Astronomy* Vol. 13 (AIP, New York, 1993)].
[29] H. R. Dullin and A. Wittek, J. Phys. A **28**, 7157 (1995).
[30] Y. Hagihara, *Celestial Mechanics, Vol. IV, Parts 1,2: Periodic and Quasi-Periodic Solutions*, Japan Society for the Promotion of Science (Tokyo, 1975), p. 1243.
[31] S. Bleher, C. Grebogi, E. Ott, and R. Brown, Phys. Rev. A **38**, 930 (1988).
[32] A. P. S. de Moura and C. Grebogi, Phys. Rev. E **66**, 046214 (2002).
[33] J. Schneider, T. Tél, and Z. Neufeld, Phys. Rev. E **66**, 066218 (2002).
[34] M. Hénon, Astron. Astrophys. **9**, 24 (1970).
[35] A. D. Bruno, *The Restricted 3-Body Problem* (Walter de Gruyter, Berlin, 1994).
[36] J. Nagler (unpublished).

[37] H. Yoshida, Phys. Lett. A **150**, 262 (1990).
[38] M. Preto, S. Tremaine, Astron. J. **118**, 2532 (1999).
[39] J. Schneider and T. Tél, Ocean Dyn. **53**, 64 (2003).
[40] I. Tuval, J. Schneider, O. Piro, and T. Tél, Europhys. Lett. **65**, 633 (2004).
[41] W. H. Jefferys, *An Atlas of Surfaces of Section for the Restricted Problem of Three Bodies* (Publications, Department of Astronomy, University of Texas, Austin 1971).